Visualization of Gas-Oil-Water Flow in Horizontal Pipeline Using Dual-Modality Electrical Tomographic Systems

Qiang Wang, Mi Wang, Kent Wei, and Changhua Qiu

***Abstract*—Employing dual-modality tomography inherently involves data from multiple dimensions, and thus a coherent approach is required to fully exploit the information from various dimensions. This paper describes a novel approach for dual-modality electrical resistance and capacitance tomography (ERT-ECT) to visualize gas-oil-water flow in horizontal pipeline. Compared to conventional methods with dual-modality tomographic systems, the approach based on thresholding takes account of multi-dimensional data, which therefore is capable of providing insights into investigated flow in both spatial and temporal terms. The experimental results demonstrate the feasibility of the approach, by which 6 common flow regimes in horizontal pipeline flow are visualized based on the multi-dimensional data with ERT-ECT systems, including (wavy) stratified flow, plug flow, slug flow, annular flow and bubbly flow. Although the present approach is proposed for data acquired with ERT-ECT system, it is potentially adaptable to other dual-modality tomographic systems that use concentration tomograms as inputs.**

***Index Terms*—Dual-modality electrical tomography, multi-phase flow measurement and visualization, multi-dimensional data fusion, flow regimes visualization.**

I. Introduction

GAS-OIL-WATER flow is a common phenomenon in many industrial sectors, e.g. petroleum engineering, but measuring and visualizing such flow is extremely challenging due to the complex interactions between each phase and optical opaque in nature. Conventional optical methods, e.g. high-speed videos, are the most straightforward solution, but their applicability is reliant on the availability of appropriate conditions, e.g. observation section. In addition, it was also reported that when gas volume fraction is larger than 10% the methods are no longer feasible due to a large number of opaque bubbles [1]. Another feasible way is the applications of multi-modality tomographic systems, i.e. simultaneously applying multiple modalities to decompose each phase in the flow [2], [3].

Dual-modality tomographic systems (DMTS), i.e. an integration of multiple tomographic techniques, have attracted many research interests and been proposed for the measurement and visualization of multiphase flow in the past few decades [4]–[7]. The primary purpose of DMTS can be into two groups: one is for improving the relatively low spatial resolution by single-modality tomographic system (SMTS). For example, Zhang et al. [8] integrated ECT with Gamma-ray computerized tomography (GCT) to gain high-resolution images. The other group is for overcoming the incapability of SMTS for distinguishing individual components involved in a mixture containing more than two components, e.g. gas, oil, and water components in three-phase flow. An exemplary application was performed combining ECT and magnetic inductance tomography (MIT) systems to image static objects in a phantom [9]. Hjertaker et al. [10] also proved that ECT and gamma-ray systems are capable of demonstrating phase distributions in gas-oil-water hydrocarbon flow. In addition, dual-modality wire mesh sensor was proposed for the visualization of simulated gas-oil-water horizontal flow [11].

A particular group of DMTS is ERT-ECT systems, which are characterized by low-cost, non-intrusive/invasive and non-radioactive electrical tomography. They usually offer tomograms with high temporal resolution, at sub-millisecond [12], [13] but relatively low spatial resolution up to 5% [6], [14]. A number of efforts have been made to explore the application of dual-modality ERT-ECT systems for multiphase flow imaging, such as gas-liquid two-phase flow or gas-oil-water three-phase flow. [6], [15]–[19]. Although those systems are electrical tomography, they have their own unique features. Some of them employ two standalone modalities to obtain conductivity and permittivity distributions [6], while some others measure impedance in a non-intrusive way to derive conductivity and permittivity simultaneously [19]. An interesting example of ERT-ECT systems is an ECT-based system [15], [20], which measures capacitance for permittivity imaging and power balance for conductivity imaging. Since the sensors are mounted on the outer surface of a pipe, it works non-invasively.

The engagement of DMTS always requires the methods that allow the data in multiple dimensions to be fused effectively, including, but not limited to, space, time, and frequency [3], [4]. Spatial fusion involves the geometrical combination of the images at different time and/or from different modes, and thus is critical for resolving the phase distributions [3], [21]. Temporal fusion engages the transformation of local times by each mode to a common time axis, so that the images to be fused reflect the interested objects happened at the same time [21]. Since temporal contents are linked with the properties under most investigations, temporal fusion is critical for reflecting property dynamics [3]. Energy fusion concerns the integration of the data, i.e. properties of interests, from two or more modes, or from one mode with different excitation

Q. Wang, and M. Wang are with the School of Chemical and Process Engineering, University of Leeds, Leeds LS2 9JT, UK (E-mail: m.wang@leeds.ac.uk).

K. Wei, and C. Qiu are with Industrial Tomography System plc, Manchester M3 3JZ, UK.

frequency [3], of which the properties are responsible for the decomposition of different phases.

Due to the involvement of reconstruction process in tomographic systems, fusion could happen before, during or after reconstruction. However, fusion performed before reconstruction, i.e. raw data-based fusion, is, unfortunately, not available so far [22]. Fusion performed during reconstruction, i.e. reconstruction-level fusion, happens when reconstruction by one tomographic mode utilizes the reconstructed information from the other tomographic mode, and the reconstructed images at second step are able to interpret desired phase distributions, and ideally no further process is needed. However, pure reconstruction-level fusion is, to our best knowledge, unavailable, neither. Zhang et al. [9] partially applied reconstruction-level fusion in their approach by using MIT produced images to update the forward model in ECT reconstruction, but further image-based fusion still required after the reconstruction. Fusion performed after reconstruction, i.e. image-based fusion, combines the tomograms reconstructed separately by each mode. Image-based fusion is the most widely applied approach for DMTS, due to the computational and implementational simplicity. In this case, reconstructed data can be fused simply using thresholding [6], [8], [11], [16], [18], [22], or employing advanced algorithms, such as fuzzy logic [23] or fuzzy c-means (FCM) [17].

From data fusion perspective, various advanced techniques have been proposed, especially in medical imaging [24], which shares some common characteristics with process tomography, such as sensing modalities. It seems that data fusion in multiphase flow imaging is trivial because those mature techniques in medical imaging could be applied directly. This, however, introduces several technical challenges, rising from the requirements for qualification of flow dynamics. For example, electrical tomography, due to its relative low spatial resolution, is limited in indication of small bubbles or clear boundaries of large air bubbles in liquid. In addition, quantification, e.g. component concentration, is mandatory in the application, and hence performance evaluation is often built upon flow quantitative comparison between fused outcome and reference, rather than those used in medical imaging fusion.

As far as DMTS-based gas-oil-water flow visualization is concerned, conventional approaches have been evaluated by simulations and preliminary experiments, e.g. using statically-positioned objects or the flows with simple structures. The majority of them took account of the fusion at spatial and frequency level, but excluding temporal data, [6], [16], [17], and hence were only able to reveal limited information regarding flow regimes. Although others integrated aforementioned multi-dimensional contents [11], [23], their applicabilities were still restricted to slug flow and annular flow. To our best knowledge, no existing method has been evaluated by real-world industrial cases. Another insufficiency in this field is the lack of explicit formalization of data fusion scheme, where most of them rely on empirical knowledge to implicitly perform data fusion.

In this paper, a visualization approach based on multi-dimensional data fusion of dual-modality ERT-ECT measurements for gas-oil-water flow in an industrial horizontal pipeline is reported. The approach integrates the data from spatial, temporal and frequency dimensions, and thus is able to convey the informative contents in regard to phase distributions and flow regimes. Evaluation using industry-scale testing facilities proves the feasibility of the approach by visualizing common flow regimes in horizontal pipeline, including (wavy) stratified flow, plug flow, slug flow, annular flow, and bubbly flow. Although the approach was proposed for ERT-ECT systems, it could be easily adapted to other DMTS, with little or even without effort.

The rest of the paper are organized as follows. Section II introduces the background with respect to the dual-modality ERT-ECT systems used for the investigation, and common flow regimes for gas-oil-water horizontal flow. The visualization approach is comprehensively explained in Section III, and evaluated in Section IV. The conclusion is given in Section V.

II. Background

A. Dual-modality ERT-ECT systems

Electrical tomography is a technique that utilizes electromagnetic principles to sense the electrical property distribution within the sensing domain. Different tomography methods have different sensitive properties, depending on its operation principles. For example, ERT utilizes the variation of conduction current to detect the process variation, hence the measurements are mainly dominated by electrical conductivity changes within the sensor. In contrast, ECT utilizes the variation of displacement current to sense the process variation. Its measurements are mainly affected by the electrical permittivity variation in the sensor. Because ERT and ECT have distinct sensing properties, they are often proposed to monitor multiphase processes as a dual-modality system. Fig. 1 shows a typical concept of using an ERT-ECT system to monitor and control a multi-phase flow process [6].

As ERT is electrically conductivity-sensitive, under a gas/oil/water three-phase condition, it is able to separate the water phase from the non-conducting gas/oil phase. The reconstructed ERT conductivity images can determine disperse phase concentration distribution passing through the sensor, whereas for the permittivity sensitive ECT, the reconstructed permittivity image can determine the ratio between gas and liquid (mixture of oil and water) across the sensor. As the dual-modality system used in the investigation, the ERT (ITS V5R) measurements will generate a 20×20 pixels conductivity tomogram, and the ECT (ITS M3C) will generate a 30×30 permittivity tomogram. It is worth mentioning that the difference in the grid definition of ERT and ECT tomograms is because of the pre-defined sensitivity map in the ERT and ECT software that was used for generating reconstructed tomograms, rather than the characteristics of the deployed hardware. By combining both images via interpolation process, the composition of each phase within the sensor can be calculated. Fig. 2 illustrates the set-up of the dual modality system for visualization of gas-oil-water three phase flows and Table I lists the major specification of the ERT-ECT systems.

The ERT and ECT systems in the use measure the relative change instead of the absolute value of electrical property

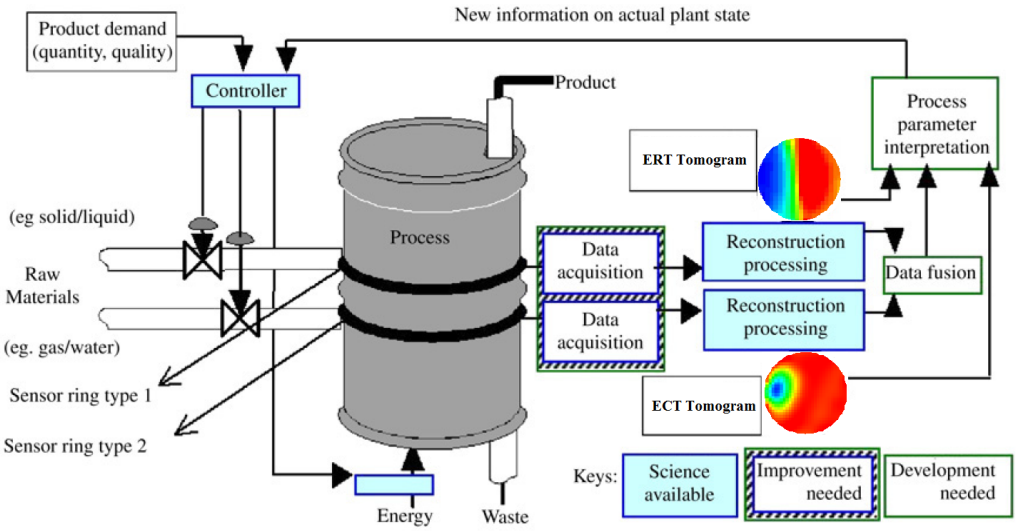

Fig. 1. A typical industrial need of a dual-modality tomography system [6].

TABLE I
OPERATION SPECIFICATION OF THE ERT-ECT SYSTEMS.

	V5R	M3C
Sensor configuration	2 planes of 16 electrodes	1 plane of 12 electrodes
Sensing strategy	Voltage-driven adjacent	Voltage-driven sequential
Injection frequency	0.01 MHz	1 MHz
Reconstruction	Linear back projection (LBP)	Linear back projection (LBP)
Property of interest	Electrical conductivity	Electrical permittivity
Max acquisition speed	16 ms/Frame	100 ms/Frame
Image spatial resolution	5%	5%
Admittance sensitivity	1% (5μS/cm in 500μS/cm water)	1% (8.85e-14 F/m in air)

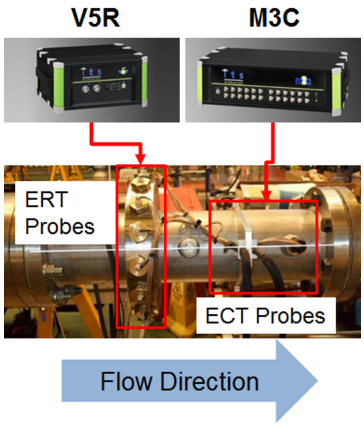

Fig. 2. ERT-ECT systems and integrated sensors used in the experiment [6].

distribution. Then, the phase concentration information in reconstructed tomograms is derived with the effective medium approximations equations such as Maxwell Garnett theory [25], which reflect the non-linear behaviour of the mixtures electric property to phase concentration. For the instance of oil-water two phase mixture, ERT can well handle the water continuous mixture since the effect of permittivity can be treated as ignorable at the low excitation frequency. However, ECT may produce considerable error even in the oil continuous mixture since the high permittivity of water, which can potentially saturate the measurement signal. Nevertheless, for the three-phase flow under the investigation, a large permittivity difference between gas and oil/water or large conductivity difference between water and gas/oil exist. Therefore, ECT permittivity image is reconstructed to report gas in liquid and ERT conductivity image to report gas and oil in water. With the sum of phase volume fractions equal to 1, the oil phase distribution can be derived approximately.

B. Gas-oil-water flow regimes in horizontal pipeline

When another immiscible phase is introduced into gas-liquid flow, flow patterns become extremely complicated. The observable flow regimes for gas-oil-water flow in horizontal pipeline can be over 20 [26]–[29]. To limit the scope of the study, there were totally 6 targeting flow regimes to be examined, including (wavy) stratified, plug, slug, annular, and bubbly flow [20, 21]. In consequence, only these 6 flow patterns are concerned. Fig. 3 illustrates an example of aforementioned 6 interested flow regimes of gas-liquid horizontal flow, and describe as following:

- *Stratified flow* occurs when gas phase and liquid phase are completely separated (Fig. 3a);

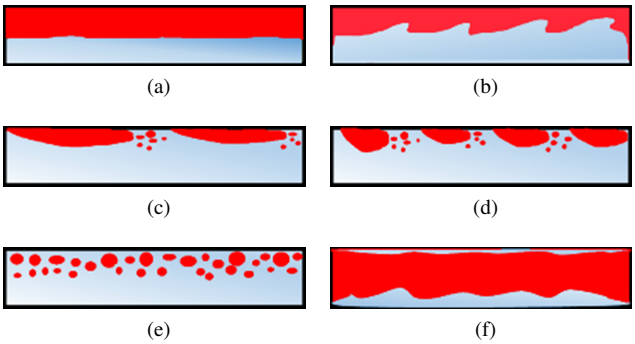

Fig. 3. 6 common flow regimes of gas-liquid flow in horizontal pipeline. (a) stratified flow; (b) wavy stratified flow; (c) slug flow; (d) plug flow; (e) bubbly flow; and (f) annular flow.

- *Wavy stratified flow* is characterized by appearance of waves along gas and liquid interface (Fig. 3b);
- *Slug flow* becomes visible when waves frequently touch the top wall. Accordingly, gas is not continuous anymore and split to long bubbles, between which there are usually some dispersed bubbles (Fig. 3c);
- *Plug flow* appears when there are elongated bubbles at the top of the pipe, while liquid flows at the bottom of the pipe, between which there may be dispersed (Fig. 3d). Sometimes, a thin liquid film between the elongated bubbles and top wall of the pipe [30];
- *Bubbly flow* happens when gas phase is fully dispersed and exists as small bubbles at the top of the pipe (Fig. 3e); and
- *Annular flow* exists when gas phase floats at the center of the pipe, and two thin liquid films appear between the gas and the pipe (Fig. 3f). Due to the gravitational force, the upper liquid film is usually much thinner than lower film [30].

III. Approach

Since concentration tomograms[1] by ERT and ECT are different in spatial and temporal terms, they have to be spatially and temporally aligned before the fusion. After the alignment, the tomograms are fused on a pixel-by-pixel basis, which are then visualized using conventional color mapping method. The data flow of the approach is depicted in Fig. 4, and each step in Fig. 4 will be explained in the following sections.

A. Data pre-processing

Before pre-processing the data, conductivity and permittivity tomograms are firstly reconstructed in respect to ERT and ECT [31]. The tomograms are further converted to concentration tomograms by Maxwell equation as an inherent function of the software. The ERT concentration tomograms reflect the concentration distribution of disperse phase, i.e. gas and oil in this study, whereas the ECT concentration tomograms represent the concentration distribution of gas phase. These two sets of concentration tomograms are further processed by the proposed approach. Since the ERT and the ECT work at different frequency and produce tomograms with different mesh definitions, resulting in the concentration tomograms with different spatial and temporal resolution, the concentration tomograms have to be transformed to a common coordinate system before data fusion. In our case, linear interpolation is employed because it is simple to be implemented and requires little computing power.

Since the systems are deployed on the same pipe, both grids, i.e. 20×20 for the ERT and 30×30 for the ECT, represent the same physical area, i.e. cross-section of a pipe. Therefore, they need to be resampled to a new grid, where the definition is determined by the least common multiple of the original grids. The principle of the applied spatial alignment is demonstrated in Fig. 5a, in which ERT tomograms $C^{M^{ERT,s}}$ with the mesh of $N^{ERT} \times N^{ERT}$ and ECT tomograms $C^{M^{ECT,s}}$ with the mesh of $N^{ECT} \times N^{ECT}$ are resampled to the new tomograms with the same mesh of $N^{lcm} \times N^{lcm}$, where N^{lcm} is determined by the least common multiple of N^{ERT} and N^{ECT}, i.e. $N^{lcm} = LCM(N^{ERT}, N^{ECT})$. In this study, both ERT grid (20×20) and ECT grid (30×30) are transferred to a grid size of 60×60. Fig. 5b depicts an example of the spatial alignment for a pipe with 60mm diameter, in which the pixel in the ERT tomogram represents an area of (60/20)mm×(60/20)mm = 3mm×3mm of the pipe, and the ECT one is (60/30)mm×(60/30)mm = 2mm×2mm. As a result, the resampled pixels are (60/60)mm×(60/60)mm = 1mm×1mm.

As far as temporal information is concerned, the sampling frequency is fixed with a given tomography. That is, the time interval between any two consecutive tomograms by a tomographic system is constant. Let the data acquisition speed of a tomography is DAS^m frame/second (fps), i.e. DAS^{ERT} and DAS^{ECT} number of frames are collected by the ERT and the ECT for every second, respectively. If $DAS^{ERT} = DAS^{ECT}$, temporal alignment is unnecessary, or otherwise is demanded. Since the interval is constant, a similar strategy for the spatial alignment can be applied for temporal alignment. In other words, let DAS^{lcm} is the least common multiple of the DAS^{ERT} and DAS^{ECT}, i.e. $DAS^{lcm} = LCM(DAS^{ERT}, DAS^{ECT})$, and T_t is the temporal transform function, which is conceptually defined as $T_t : F^{DAS^m} \rightarrow F^{DAS^{lcm}}$. By the transformation, a DAS^m number of the original frames are resampled into a DAS^{lcm} number of the targeting frames, and thus the frames from each tomography are temporally aligned. Fig. 6 depicts the temporal alignment in this study, in which $DAS^{ERT} = 62.5$ and $DAS^{ECT} = 12.5$, and hence $DAS^{lcm} = 5$. As a result, three frames $F'^{ECT}_{(n\times DAS^{ECT}+1)}$, $F'^{ECT}_{(n\times DAS^{ECT}+2)}$, and $F'^{ECT}_{(n\times DAS^{ECT}+3)}$ are interpolated into the original two ECT tomograms between $F^{ECT}_{(n\times DAS^{ECT}+1)}$ and $F^{ECT}_{(n\times DAS^{ECT}+2)}$.

At this point, the original two sets of tomograms are transformed into another two sets of tomograms which are spatially and temporally aligned. Each tomogram has the same spatial resolution of $M = N^{lcm} \times N^{lcm}$, where $N^{lcm} = LCM(N^{ERT}, N^{ECT})$. In addition, the numbers of the tomograms by each modality is identical and dis-

[1]The terms *data*, *tomograms*, and *images* refer to cross-sectional concentration distribution, unless otherwise specified.

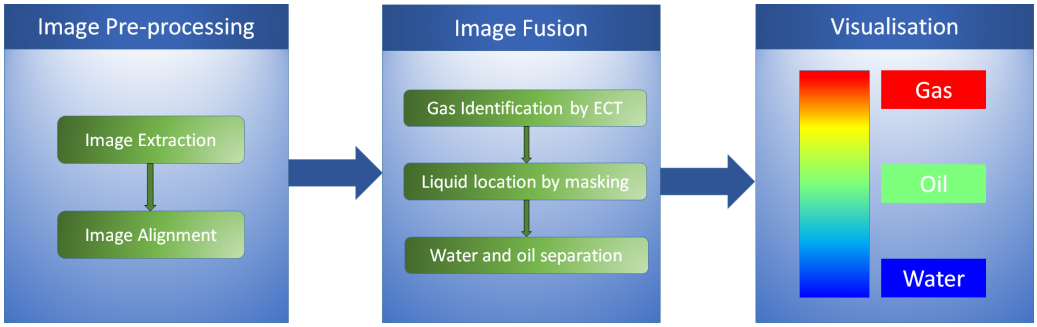

Fig. 4. Schematic diagram of fusion procedure

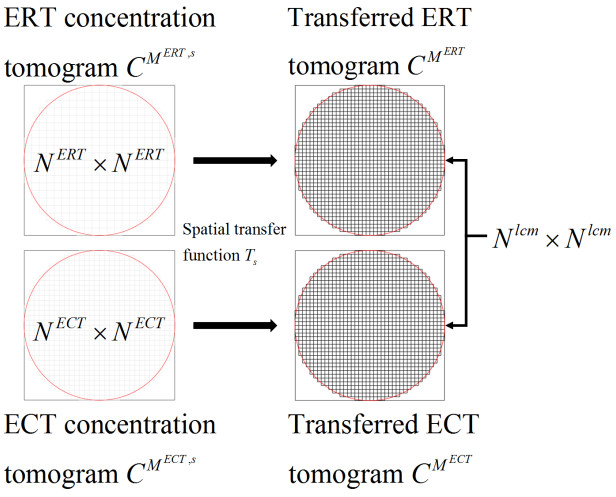

(a)

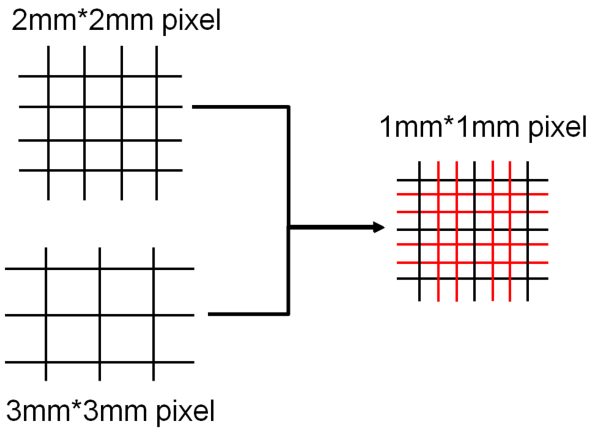

(b)

Fig. 5. (a) principle of spatial alignment; and (b)an example of 20×20 ERT tomograms and 30×30 ECT tomograms to 60×60 tomograms.

tributed homogeneously along temporal axis, where there are $DAS^{lcm} = LCM(DAS^{ERT}, DAS^{ECT})$ number of tomograms per second. The aligned tomograms are used as the input for next step.

Let $T^m = \{F^{i,m} \mid i \in \{1, 2, \cdots, Q\}\}$ denote two sets of aligned concentration tomograms, where m is ERT or ECT to represent different modalities. Let $C^{i,m} = \{c_x^{i,m} \mid x \in \{1, 2, \cdots, N^{lcm} \times N^{lcm}\}\}$ denote ith two-dimensional cross-sectional concentration tomogram with spatial resolution of $N \times N$. The resultant axially-stacked tomograms can be written as:

$$S^m = \{s_{x,y}^m \mid s_{x,y}^m = \frac{1}{A}\sum_{a=1}^{A} c_{idx+(a-1)\times m}^{y,m}, \quad x \in \{1, \cdots, N^{lcm}\}, y \in \{1, \cdots, Q\}\} \tag{1}$$

where *idx* is the starting index of the selected central area in a tomogram, and A is the number of columns to be averaged in the central area. Fig. 7 demonstrates an example of generating an axially-stacked image. In Fig. 7, a Q number of cross-sectional tomograms $F^{Q,m}$ are aligned for a modality m in the interval of $[T_0, T_n]$. In order to generated the axially-stacked tomogram, the data in the central four columns (the blue area) of each cross-sectional tomogram is extracted, shown as the arrow 1, and then row data are averaged to approximate the original spatial information, depicted by the arrow 2. Finally, all spatial information is arranged sequentially to produce the axially-stacked image, which is further used for the proposed fusion algorithm.

B. Data fusion

The principle behind the data fusion is on the basis that using ECT to distinguish gas from water and oil, and using ERT to distinguish water from gas and oil [6], [16], [18]. Let $F = \{f_{x,y} \mid x \in \{1, 2, \cdots, N^{lcm}\}, y \in \{1, 2, \cdots, Q\}\}$ denote the fused data, and $(s_{x,y}^X)'$ denote the pixel concentration value from ERT and ECT at (x, y). $f_{x,y}$ can be calculated with (2):

$$f_{x,y} = \begin{cases} 2 & (s_{x,y}^{ECT})' \geq T_g^{ECT} \\ 0 & (s_{x,y}^{ERT})' \leq T_w^{ERT} \\ (s_{x,y}^{ERT})' & otherwise \end{cases} \tag{2}$$

where T_g^{ECT} and T_w^{ERT} are two critical threshold values that determine the occupation of the pixel $f_{x,y}$. Fig. 8 depicts the data flow of the fusion.

Since for every pixel $p_{x,y}$ in the fused result F, phase composition can be described as:

$$p_{x,y} = (\alpha_{x,y}^g, \alpha_{x,y}^o, \alpha_{x,y}^w); \ \alpha_{x,y}^x \in [0, 1]; \tag{3}$$

where $\alpha_{x,y}^x$ represents local pixel concentration of the phase x, which satisfies:

$$\alpha_{x,y}^g + \alpha_{x,y}^o + \alpha_{x,y}^w = 1 \tag{4}$$

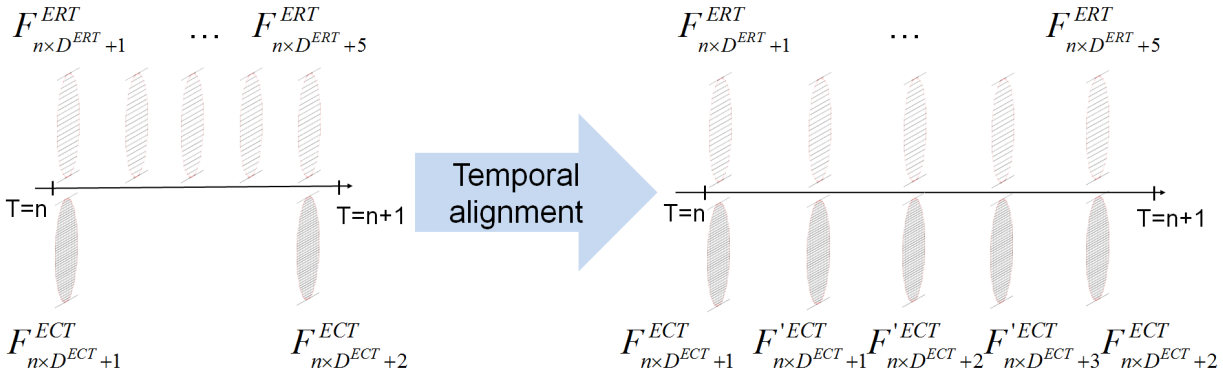

Fig. 6. Temporal alignment of the tomograms by the ERT and ECT.

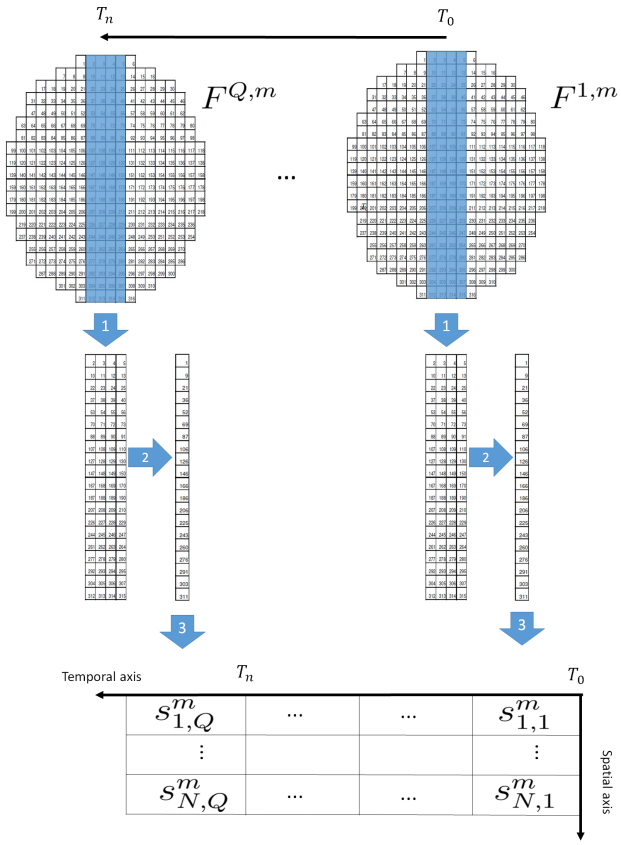

Fig. 7. Axial stacked images generated from two-dimensional cross-sectional tomograms.

Let $P = \{p_{x,y} \mid x \in \{1, 2, \cdots, N^{lcm}\},\ y \in \{1, 2, \cdots, Q\}\}$ denote the decomposed pixel concentration. Based on (2), (3), and (4), individual concentration of each phase at pixel $p_{x.y}$ can be derived by:

$$p_{x,y} = \begin{cases} (1,0,0) & f_{x,y} = 2 \\ (0,0,1) & f_{x,y} = 0 \\ (0, f_{x,y}, 1 - f_{x,y}) & otherwise \end{cases} \quad (5)$$

In the end, the ERT and ECT tomograms are integrated together, and the phases are decomposed at pixel level, which are ready for displaying.

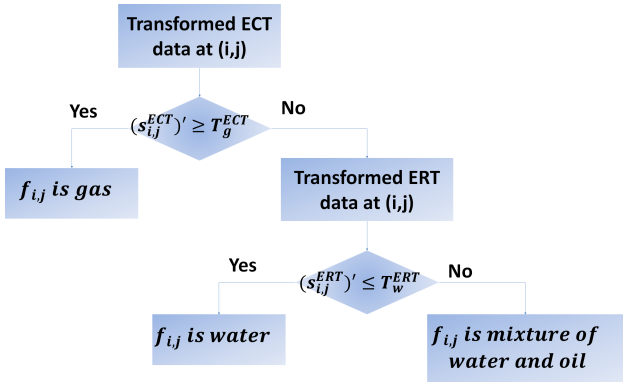

Fig. 8. Data flow of pixel-by-pixel data fusion.

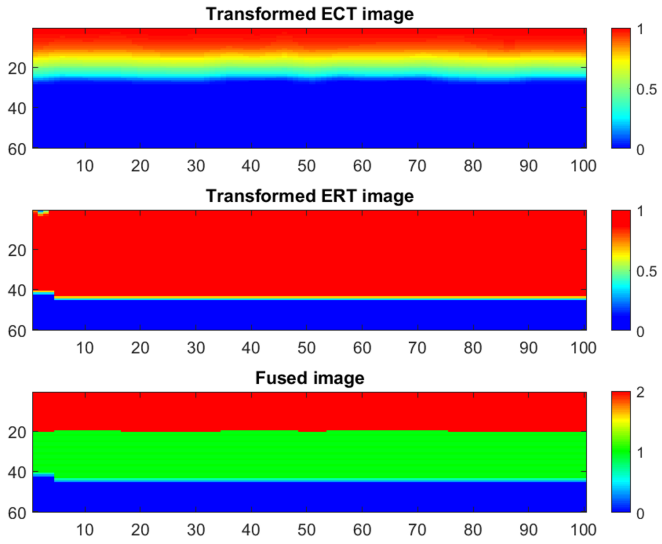

Fig. 9. An example of pixel-by-pixel data fusion over 100 tomograms of measurement time 1.6 seconds.

C. Data displaying

A predominant visualisation approach for scalar data is color mapping, i.e. transferring scalar data to different colors in line with a lookup table. A colour space $C = \{c_{x,y} \mid x \in \{1, 2, \cdots, N^{lcm}\}, y \in \{1, 2, \cdots, Q\}\}$ for the fused tomogram

can be defined as:

$$c_{x,y} = (r_{x,y}, g_{x,y}, b_{x,y}),\ r_{x,y},\ g_{x,y},\ b_{x,y} \in [0, 255] \quad (6)$$

where *r*, *g*, and *b* are the fundamental colors in RGB space, i.e. red, green, and blue. Based on (5) and (6), a transfer function T can be defined using matrix multiplication:

$$[r_{x,y}\ g_{x,y}\ b_{x,y}] = [\alpha^g_{x,y}\ \alpha^o_{x,y}\ \alpha^w_{x,y}] \begin{bmatrix} 255 & 0 & 0 \\ 0 & 255 & 0 \\ 0 & 0 & 255 \end{bmatrix} \quad (7)$$

When the pixel concentration $p_{x,y}$ is continuous, a triangle color space in [32] should be applied to reflect continuous distribution of phase concentration, whereas if it is discrete, like the one in this study, a conventional color bar is sufficient to reveal the concentration distribution of fused results. Fig. 9 demonstrates an example, in which transformed ECT and ERT images, and fused image with equivalent sampling rate over 1.6 seconds, from top to bottom, are presented. In the fused image (the bottom one) based on the transformed ECT (the top one) and ERT (the middle one) images, three different phases are illustrated by three different colors, where the red is gas, the green is oil, and the blue is water.

IV. Evaluation

Before the approach is evaluated, two critical threshold values need to be addressed firstly. It was reported that systematic error produced by ERT system is less than 5% [14]. Therefore, when measured concentration is less than 5 %, the corresponding phase is assumed as pure water. Therefore, T_w^{ERT} is set to 0.05 for the ERT. The determination of T_g^{ECT} is quite challenging due to the difficulty from theoretical estimation. In [6], an empirical implicit threshold value 0.5 was utilized to distinguish gas from liquid phase, which showed acceptable outcome from both measurement and visualization point of view. In addition, central values are commonly used as a criterion for interface detection [33], [34]. Therefore, a central value of ECT concentration tomograms 0.5 is applied in this report as the threshold value T_g^{ECT} to extract gas phase from the ECT.

A. Experimental setup

The experiments were conducted using industry-scale gas-oil-water flow facilities at TUV NEL UK [2]. A 4-inch pipe was deployed for the experiments. On the test section, ITS M3C ECT system [6] and V5R ERT system [35] were utilized, locating approximately 50 m from the injection points. A high-speed camera was also utilized to record flow structures for all tested flow conditions through a transparent photo chamber. The arrangement of corresponding sensors on test section is depicted in Fig. 10.

In the experiments, nitrogen was utilized as gas phase, Paraflex (HT9) was as oil phase, and salty water was as water phase, with pressure at 10 bars and temperature at 20 degree. The physical properties of each phase is listed in Table II. Since the tested flow conditions involved water-cuts from 0% to 100%, combined with gas volume fraction (GVF) from 0% to 100%, it was able to produce common flow regimes in horizontal pipe, covering (wavy) stratified flow, plug flow, slug flow, annular flow and bubbly flow. In this paper, one flow condition for each flow regime was selected for the evaluation of the proposed visualization approach. The detailed information with regard to the selected flow conditions is specified in Table III. It should be notified that the measured mean concentrations are based on local tomograms. Since phase velocities and local pressure at the sensing location were not measured during the experiments, hence the local volume fraction of each phase are unable to be derived. Nevertheless, the comparison between the measured mean concentrations and the volume fractions from Water-cuts and GVF would still provide useful information due to their obvious correlation. To avoid potential confusion, hereafter, the terms of *void fraction* and *volume fraction* are used to correspond the local mean concentration at sensing location and reference volume fraction at feed-in point, respectively.

[2]http://www.tuvnel.com/

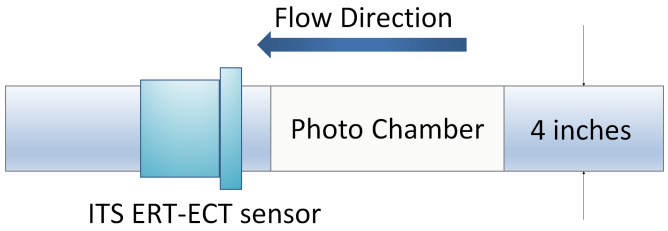

Fig. 10. Arrangement of testing facilities.

TABLE II
Physical properties of each phase.

	Gas	Oil	Water
Fluid	Nitrogen	Paraflex	Salty water
Conductivity (mS/cm)	0	0	33.5
Dielectric constant (ε)	1	2.2	80
Dynamic viscosity (cP)	0.0174	16.18	1.35
Density (kg/m^3)	12	830	1049.1

B. Visualization results

Fig. 11 to Fig. 16 present the visualization results by the proposed approach using aforementioned threshold values, along with relating photos taken during the experiment through the viewing section, where the red, green and blue color in fused image denote air, oil and water, respectively. The photos were produced by connecting a few screenshots taken during the play. The visualization results were rendered using conventional color mapping, in which the red represents the gas, the green represents the oil, and the blue represents the water. In each figure, frames in different number were stacked for better view of flow regimes based on flow conditions and photos.

From visualization perspective, the results clearly identify individual phase when all phases are separated in Fig. 11, Fig. 12, and Fig. 13. The results in Fig. 14 and Fig. 15 also

TABLE III
SELECTED FLOW REGIMES WITH FLOW CONDITION REFERENCES FOR THE EVALUATION OF THE PROPOSED VISUALIZATION APPROACH.

Observed flow regime	Water-cuts (%)	GVF (%)	Q_{gas} (l/s)	Q_{oil} (l/s)	Q_{water} (l/s)
Stratified flow	50	60	3.13	1.04	1.04
Wavy stratified flow	75	40	1.39	0.52	1.56
Slug flow	75	42	3.62	1.25	3.75
Plug flow	75	5	1.24	5.90	17.71
Annular flow	90	92	127.78	1.11	10.00
Bubbly flow	90	35	20.94	3.89	35.00

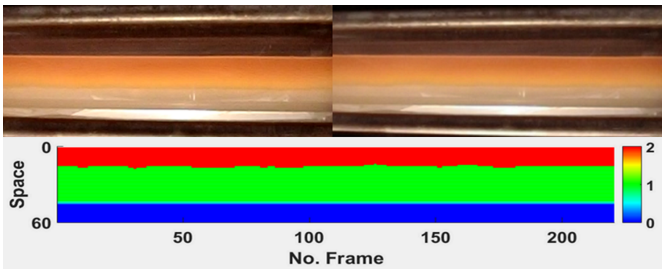

Fig. 11. Visualization result of stratified flow over 250 frames of measurement time 7 seconds.

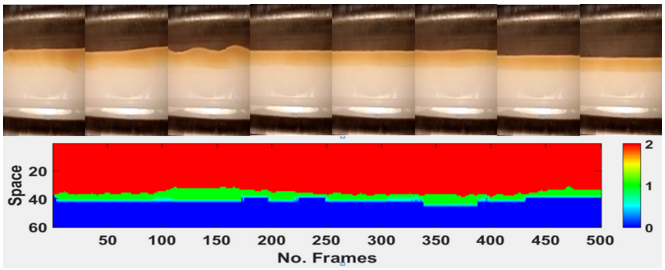

Fig. 12. Visualization result of wavy stratified flow over 500 frames of measurement time 8 seconds.

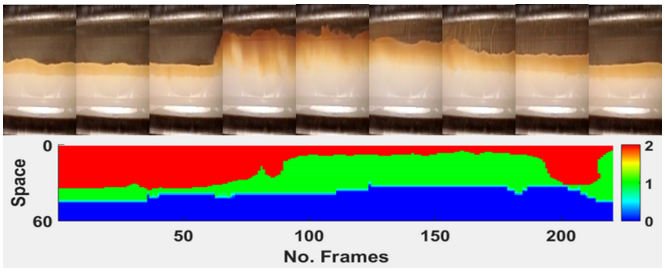

Fig. 13. Visualization result of slug flow over 200 frames of measurement time 3.2 seconds.

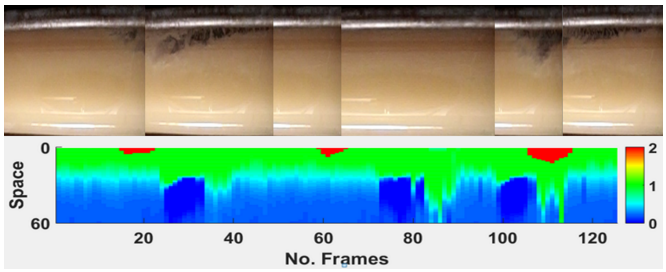

Fig. 14. Visualization result of plug flow over 125 frames of measurement time 2 seconds.

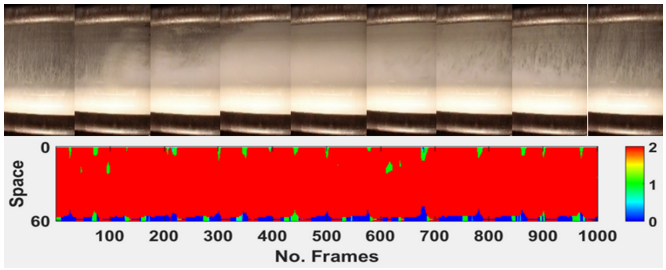

Fig. 15. Visualization result of annular flow over 1000 frames of measurement time 16 seconds.

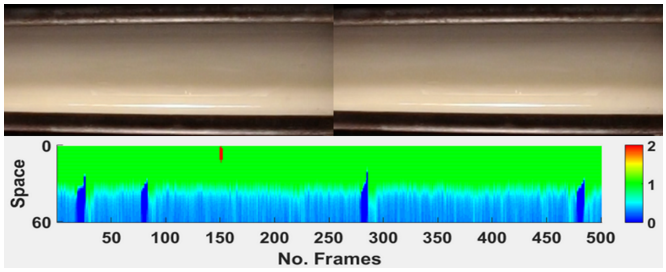

Fig. 16. Visualization result of bubbly flow over 500 frames of measurement time 8 seconds.

have good agreement with the corresponding photos. Unfortunately, dispersed bubbles are unable to be identified due to the relatively low spatial resolution of electrical tomography. Thus, the gas phase in bubbly flow is less distinguishable, as depicted in Fig. 16.

On the other hand, the threshold T_g^{ECT} plays a critical role in the determination of gas phase distribution, which further influences the visualization results, since the selected value is empirical. Therefore, the impact of the threshold on the concentration and visualization is also evaluated under one flow regime. Fig. 17 and Fig. 18 illustrate the comparison. Five different thresholds were applied, including 0.3, 0.4, 0.5, 0.6, and 0.7. Fig. 17 presents the mean concentration of each phase by 5 different thresholds, and the true values of each phase are also included as reference. It is apparent from Fig. 17 that the higher the threshold is, the less the gas phase is, which in turn lowers oil concentration. This effect is also reflected by Fig. 18, in terms of the areas of the green and the red. In general, the gas phase is purely determined by the relating threshold based on ECT tomograms, whereas the oil phase is extracted on the basis of ERT and ECT tomograms. When the water threshold remains the same, the sum of the gas and the

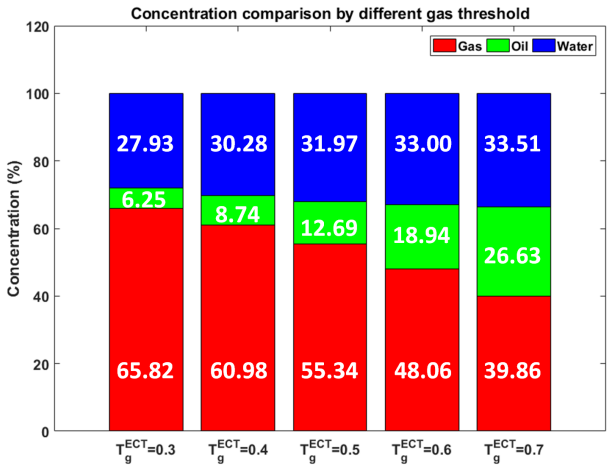

Fig. 17. Comparison of phase concentrations using different threshold T_g^{ECT}.

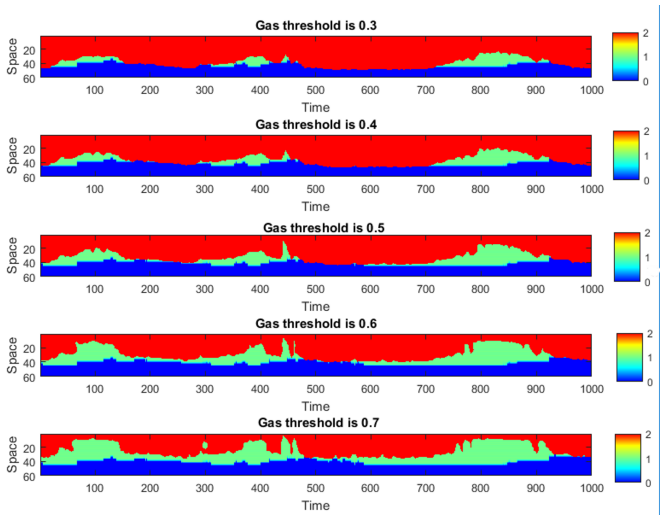

Fig. 18. Comparison of visualization using different threshold T_g^{ECT} over 1000 frames of measurement time 16 seconds.

oil phases changes unnoticeably. Accordingly, when the gas threshold increases, its concentration decreases, whereas the water concentration rises.

The phase composition information is also extracted from reconstructed tomograms with default thresholding value (0.05 and 0.5), as shown in Fig. 11 to Fig. 16. For each flow regime, the measured void fractions are listed in Table IV, along with the reference volume fractions based on water-cuts and GVF. The results also demonstrate that although the ERT-ECT systems are unable to visualize small bubbles, particularly in bubbly flow, as shown in Fig. 16, they are still capable of presenting quantitative results, i.e. phase concentrations. This is primarily because ECT is able to measure the existence of gas phase, e.g. non-zero mean concentrations, even though it is hardly able to reflect the size and distribution of small bubbles.

V. Conclusion

We have proposed a novel visualization approach that incorporates the information from spatial, temporal, and frequency dimensions, and evaluated the approach using industry-scale horizontal flow testing facilities. Through the approach, common flow regimes occurring in horizontal pipeline are visualized, and the results demonstrate the feasibility of our approach. The approach requires the input of two stacks of cross-sectional concentration tomograms from ECT and ERT, which potentially enables it to be a general framework for other dual-modality systems. Although the algorithm employed in the approach is a pixel-by-pixel determination of phase concentration, it is not difficult to adapt other algorithms, e.g. fuzzy logic [23] to improve the results.

However, a few aspects still need further efforts. Firstly, the threshold value T_g^{ECT} deserves a theoretical and experimental investigation owing to its considerable significance in determining gas phase. In addition, ambiguous visualization of bubbly flow should also be addressed. The ambiguity could be relieved by improving the spatial resolution of reconstructed tomograms, such as applying advanced iterative reconstruction algorithms, e.g. sensitivity theorem-based conjugate gradient method (SCG) [36]. Another aspect is the artificial errors introduced by the linear interpolation used in data alignment, due to the differences of DAS speed and tomogram mesh definition between ERT and ECT. The errors could be eliminated by advanced design of the hardware, such as the one in [18], where conductance and capacitance were measured simultaneously, and hence, at least, temporal registration is not compulsory.

Acknowledgment

The authors would like to thank the valuable comments from anonymous reviewers. The authors also appreciate the financial supports by the Engineering and Physical Sciences Research Council (EP/H023054/1), IAA (ID101204), and the European Metrology Research Programme (EMRP) project Multiphase flow metrology in the Oil and Gas production, which is jointly funded by the European Commission and participating countries within Euramet and the European Union.

References

[1] D. S. H.M. Prasser and C. Zippe, "Bubble size measurement using wire-mesh sensors," *Flow Measurement and Instrumentation*, vol. 12, no. 4, pp. 299 – 312, 2001.

[2] T. York, H. McCann, and K. B. Ozanyan, "Agile sensing systems for tomography," *IEEE Sensors Journal*, vol. 11, no. 12, pp. 3086–3105, Dec 2011.

[3] B. S. Hoyle and M. Wang, "Multi-dimensional opportunities and data fusion in industrial process tomography," in *Instrumentation and Measurement Technology Conference (I2MTC), 2012 IEEE International*, May 2012, pp. 916–920.

[4] R. West and R. Williams, "Opportunities for data fusion in multi-modality tomography," in *1st World Congress Industrial Process Tomography*, 1999, pp. 195–200.

[5] B. Hoyle, X. Jia, F. Podd, H. Schlaberg, H. Tan, M. Wang, R. W. R.M. West, and T. York, "Design and application of a multi-modal process tomography system," *Measurement Science and Technology*, vol. 12, no. 8, p. 1157, 2001.

[6] C. Qiu, B. Hoyle, and F. Podd, "Engineering and application of a dual-modality process tomography system," *Flow Measurement and Instrumentation*, vol. 18, no. 56, pp. 247 – 254, 2007, process Tomography and Flow Visualization.

[7] M. Wang, J. Jia, Y. Faraj, Q. Wang, C. Xie, G. Oddie, K. Primrose, and C. Qiu, "A new visualisation and measurement technology for water continuous multiphase flows," *Flow Measurement and Instrumentation*, vol. 46, Part B, pp. 204 – 212, 2015, special issue on Tomography Measurement & Modeling of Multiphase Flows.

TABLE IV
PHASE CONCENTRATION QUANTIFICATION RESULTS FOR DIFFERENT FLOW REGIMES.

		Gas	Oil	Water
Stratified Flow	Reference volume fraction (%)	40.00	30.00	30.00
	Fused void fraction (%)	44.21	23.56	32.24
Wavy stratified flow	Reference volume fraction (%)	60.00	10.00	30.00
	Fused void fraction (%)	59.73	4.21	36.06
Slug flow	Reference volume fraction (%)	42.00	14.50	43.50
	Fused void fraction (%)	60.11	5.60	34.29
Plug flow	Reference volume fraction (%)	5.00	24.00	71.00
	Fused void fraction (%)	6.23	23.76	70.01
Annular flow	Reference volume fraction (%)	92.00	0.80	7.20
	Fused void fraction (%)	95.12	1.03	3.85
Bubbly flow	Reference volume fraction (%)	35.00	6.50	58.50
	Fused void fraction (%)	16.87	26.91	56.22

[8] R. Zhang, Q. Wang, H. Wang, M. Zhang, and H. Li, "Data fusion in dual-mode tomography for imaging oil-gas two-phase flow," *Flow Measurement and Instrumentation*, vol. 37, pp. 1 – 11, 2014.

[9] M. Zhang, L. Ma, and M. Soleimani, "Dual modality ect-mit multi-phase flow imaging," *Flow Measurement and Instrumentation*, vol. 46, Part B, pp. 240 – 254, 2015, special issue on Tomography Measurement & Modeling of Multiphase Flows.

[10] B. T. Hjertaker, S. A. Tjugum, E. A. Hammer, and G. A. Johansen, "Multimodality tomography for multiphase hydrocarbon flow measurements," *IEEE Sensors Journal*, vol. 5, no. 2, pp. 153–160, April 2005.

[11] E. N. dos Santos, T. P. Vendruscolo, R. E. M. Morales, E. Schleicher, U. Hampel, and M. J. D. Silva, "Dual-modality wire-mesh sensor for the visualization of three-phase flows," *Measurement Science and Technology*, vol. 26, no. 10, p. 105302, 2015.

[12] M. Wang, Y. Ma, N. Holliday, Y. Dai, R. A. Williams, and G. Lucas, "A high-performance eit system," *Sensors Journal, IEEE*, vol. 5, no. 2, pp. 289–299, 2005.

[13] Z. Cui, H. Wang, Z. Chen, Y. Xu, and W. Yang, "A high-performance digital system for electrical capacitance tomography," *Measurement Science and Technology*, vol. 22, no. 5, p. 055503, 2011. [Online]. Available: http://stacks.iop.org/0957-0233/22/i=5/a=055503

[14] M. Wang, F. J. Dickin, and R. Mann, "Electrical resistance tomography sensing systems for industrial applications," *Chemical Engineering Communications*, vol. 175, no. 1, pp. 49–70, 1999.

[15] Q. Marashdeh, W. Warsito, L. S. Fan, and F. L. Teixeira, "A multimodal tomography system based on ect sensors," *IEEE Sensors Journal*, vol. 7, no. 3, pp. 426–433, March 2007.

[16] Y. Li and W. Yang, "Measurement of multi-phase distribution using an integrated dual-modality sensor," in *Imaging Systems and Techniques, 2009. IST '09. IEEE International Workshop on*, May 2009, pp. 335–339.

[17] S. Yue, T. Wu, J. Pan, and H. Wang, "Fuzzy clustering based et image fusion," *Inf. Fusion*, vol. 14, no. 4, pp. 487–497, Oct. 2013.

[18] J. Sun and W. Yang, "A dual-modality electrical tomography sensor for measurement of gasoilwater stratified flows," *Measurement*, vol. 66, pp. 150 – 160, 2015. [Online]. Available: http://www.sciencedirect.com/science/article/pii/S0263224115000627

[19] H. Ji, W. Tan, Z. Gui, B. Wang, Z. Huang, H. Li, and G. Wu, "A new dual-modality ect/ert technique based on c4d principle," *IEEE Transactions on Instrumentation and Measurement*, vol. 65, no. 5, pp. 1042–1050, 05 2016.

[20] Q. Marashdeh, W. Warsito, L.-S. Fan, and F. Teixeira, "Dual imaging modality of granular flow based on ect sensors," *Granular Matter*, vol. 10, no. 2, pp. 75–80, 2008. [Online]. Available: http://dx.doi.org/10.1007/s10035-007-0070-2

[21] H. B. Mitchell, *Data fusion: concepts and ideas*. Springer Science & Business Media, 2012.

[22] B. Hjertaker, R. Maad, and G. A. Johansen, "Dual-mode capacitance and gamma-ray tomography using the landweber reconstruction algorithm," *Measurement Science and Technology*, vol. 22, no. 10, p. 104002, 2011.

[23] J. Pusppanathan, M. Faramarzi, F. R. Yunus, N. M. N. Ayob, R. A. Rahim, F. A. Phang, M. H. F. Rahiman, A. Ahmad, L. P. Ling, and K. H. Abas, "Image fusion using fuzzy logic pixel fusion for dual modality tomography system," *Jurnal Teknologi*, vol. 70, no. 3, 2014.

[24] A. P. James and B. V. Dasarathy, "Medical image fusion: A survey of the state of the art," *Information Fusion*, vol. 19, pp. 4 – 19, 2014, special Issue on Information Fusion in Medical Image Computing and Systems.

[25] O. Levy and D. Stroud, "Maxwell garnett theory for mixtures of anisotropic inclusions: Application to conducting polymers," *Physical Review B*, vol. 56, no. 13, pp. 8035–8046, 1997.

[26] G. Hewitt, "Three-phase gas-liquid-liquid flows in the steady and transient states," *Nuclear Engineering and Design*, vol. 235, no. 1012, pp. 1303 – 1316, 2005, festschrift Edition Celebrating the 65th Birthday of Prof. Richard T. Lahey, Jr.20th Anniversary of Biosensors and Bioelectronicsrd International Symposium on Two Phase Modelling.

[27] C. S. C. Keskin, H. Zhang, "Identification and classification of new three-phase gas/oil/water flow patterns," in *SPE Annual Technical Conference and Exhibition*. Society of Petroleum Engineers, 2007.

[28] J. M. A. Wegmann and P. R. von Rohr, "Three phase liquid-liquid-gas flows in 5.6 mm and 7 mm inner diameter pipes," *International Journal of Multiphase Flow*, vol. 33, no. 5, pp. 484 – 497, 2007.

[29] K. E. Kee, "A study of flow patterns and surface wetting in gas-oil-water flow," Ph.D. dissertation, Department of Mechanical and Systems Engineering Russ College of Engineering and Technology Ohio University, 2014.

[30] S. Corneliussen, J.-P. Couput, E. Dahl, E. Dykesteen, K.-E. Frysa, E. Malde, H. Moestue, P. O. Moksnes, and H. T. Lex Scheers, "Handbook of multiphase flow metering," 2005. [Online]. Available: http://nfogm.no/wp-content/uploads/2014/02/MPFM_Handbook_Revision2_2005_ISBN-82-91341-89-3.pdf

[31] *ITS System 2000 Version 7.0 p2+ Electrical Resistance Tomography System - Users Manual*, Industrial Tomography Systems Plc., Speakers House, 39 Deansgate, Manchester M3 2BA, Nov. 2009.

[32] E. N. dos Santos, T. P. Vendruscolo, R. E. M. Morales, E. Schleicher, U. Hampel, and M. J. D. Silva, "Dual-modality wire-mesh sensor for the visualization of three-phase flows," *Measurement Science and Technology*, vol. 26, no. 10, p. 105302, 2015. [Online]. Available: http://stacks.iop.org/0957-0233/26/i=10/a=105302

[33] M. Misawa, N. Ichikawa, M. Akai, H. Monji, and G. Matsui, "Measurement of dynamic interface structure of slug flow in simplified rod bundles using a fast x-ray ct scanner," in *ICONE-7: Proceedings of the 7th international conference on nuclear engineering, (p. 4252)*. Japan: Japan Society of Mechanical Engineers, 1999.

[34] K. Wei, C. Qiu, M. Soleimani, and K. Primrose, "ITS reconstruction tool-suite: An inverse algorithm package for industrial process tomography," *Flow Measurement and Instrumentation*, vol. 46, Part B, pp. 292 – 302, 2015, special issue on Tomography Measurement & Modeling of Multiphase Flows.

[35] J. Jia, M. Wang, H. I. Schlaberg, and H. Li, "A novel tomographic sensing system for high electrically conductive multiphase flow measurement," *Flow Measurement and Instrumentation*, vol. 21, no. 3, pp. 184 – 190, 2010, special Issue: Validation and Data Fusion for Process Tomographic Flow Measurements.

[36] M. Wang, "Inverse solutions for electrical impedance tomography based on conjugate gradients methods," *Measurement Science and Technology*, vol. 13, no. 1, p. 101, 2002.